Journal of Physics D: Applied Physics

Amplification of near field radiation at surfaces of pure dielectric domain with anti-reflection films and photonic crystal structures

IOP Publishing Journal of Physics D: Applied Physics
J. Phys. D: Appl. Phys. **56** (2023) 245103 (10pp) https://doi.org/10.1088/1361-6463/acc8e2

Amplification of near field radiation at surfaces of pure dielectric domain with anti-reflection films and photonic crystal structures

Sy-Bor Wen* **and Aravind Jakkinapalli**

Mechanical Engineering, Texas A&M University, College Station, TX 77843, United States of America

E-mail: syborwen@tamu.edu

Received 27 October 2022, revised 16 February 2023
Accepted for publication 30 March 2023
Published 12 April 2023

Abstract

With chemical stability under high temperatures, dielectric materials can be idealized thermal emitters for different energy applications. However, dielectric materials do not support surface waves at near-infrared ranges for longer-distance thermal photon tunneling, which limits their applications in near-field thermal radiation. It is demonstrated in this study that thermal field amplification at near-infrared wavelengths at dielectric surfaces could be achieved through asymmetric Fabry–Perot resonance with anti-reflection coatings or 1D photonic crystal type structures. $\geqslant$100 nm near-infrared thermal photon tunneling can be achieved when these thin film structures are added to the emitter and the collector surfaces. Among these two thin film structures, 1D photonic crystal type periodic structures constructed with the same high refractive index material as the emitter/collector material allow near-field thermal photon tunneling at large parallel wavenumbers. Moreover, the field amplification can be increased by adding more 1D photonic crystal layers to achieve even longer distances near field thermal photon tunneling.

Keywords: antireflection, near-field, photonic crystal, photon tunneling, dielectric resonator

(Some figures may appear in colour only in the online journal)

1. Introduction

Narrowband thermophotovoltaic devices using only the radiation wavelength close to the band gap of photovoltaic (PV) cells are considered one of the potential ways of harvesting thermal energy due to the prevention of thermalization energy loss of photogenerated carriers in PV cells [1]. However, because of using narrowband radiative energy transfer in narrow band thermophotovoltaic (TPV), the resulting very small radiation flux from high-temperature emitters to the PV does not support a high fill factor of PV cells and, hence, hurts the energy conversion efficiency of TPV [2]. It is well known that radiative heat flux is proportional to the square of the refractive index of the medium [3]. Thus, radiative heat flux inside a high refractive index dielectric medium can be tens to a hundred times higher than that in free space. To use this high-intensity radiative heat flux leaked from a solid domain, especially the near-infrared wavelengths, the collector should be placed within $\sim$10 nm away from the emitter surface [4, 5]. However, the required 10 nm separation distance between the emitter and collector to efficiently harvest the radiative energy inside a solid domain is prohibitive from an engineering point of view.

It was proposed by Luo *et al* regarding two possible methods for long-distance transport of evanescent waves, the main component of the radiative energy leaked from a solid domain in the near field [6]. First, using transport material

* Author to whom any correspondence should be addressed.

supporting resonance of evanescent waves. Second, having a large optical resonance to amplify the electromagnetic field at solid interfaces in order to compensate for its exponential decay with respect to the distance, which is the method we are pursuing in this study.

It is well known that near-field thermal electric fields can be amplified at metallic surfaces at near infrared (IR) wavelengths with surface plasmon polariton, which can be harvested with PV cells. [7, 8] However, metallic surfaces can suffer from oxidation even under a vacuum environment when temperatures are close to (or higher than) 1000 K. [9] Dielectric materials, on the other hand, can be chemically stable under high temperatures. However, intrinsic dielectric material does not support surface waves at near-infrared (near IR) wavelengths. Artificial dielectric material with a high-low change in refractive indices can support Bloch surface waves in 2D/3D photonic crystals [10]. Also, high-low change in the refractive index can form asymmetric Fabry–Perot cavities supporting anti-reflection resonance [11].

In this study, we explore high-low refractive index structures in the amplification of near-field thermal electric fields at the interface to achieve a long tunneling distance of thermal photons between two dielectric domains. We especially focus on resonances induced by additional thin film dielectric structures on the emitter and the collector domains, which can be easily fabricated with current thin film deposition methods. The associated theoretical method is presented in the next section.

2. Theory

Several different methods have been established to numerically calculate near-field radiative heat transfer. For convenience, we adopted a combination of the scattering matrix method and the Wiener-Chaos expansion method demonstrated in previous studies to solve Maxwell's equations having fluctuating thermal currents semi-analytically [8, 13]. In this method, plane wave expansion is applied to decompose the electromagnetic fields into transverse electric (TE) and transverse magnetic (TM) modes. By using plane wave expansion, radiative heat flux from $z = z'$ plane of the emitter in TE and TM modes with horizontal (or parallel) wavenumbers k_x and k_y, determining the propagation direction of radiation, can be expressed as follows [12, 14]

$$\text{TE mode radiation flux } = \frac{1}{2}\text{Re}\left[\frac{1}{\omega\mu}|\boldsymbol{E}_{\text{TE}}(k_x,k_y,z')|^2 k_z^*\right] \tag{1}$$

$$\text{TM mode radiation flux } = \frac{1}{2}\text{Re}\left[\frac{1}{\omega\varepsilon}|\boldsymbol{H}_{\text{TM}}(k_x,k_y,z')|^2 k_z\right] \tag{2}$$

with $|\boldsymbol{E}_{\text{TE}}(k_x,k_y,z')|$ and $|\boldsymbol{H}_{\text{TM}}(k_x,k_y,z')|$ the amplitude of the thermal electric field in TE modes and the amplitude of the thermal magnetic field in TM modes, respectively; ω the angular frequency of the radiation; ε and μ the permittivity and permeability of the emitter; $k_z = \sqrt{\omega^2\varepsilon\mu - k_x^2 - k_y^2}$; '*' the complex conjugate. Spectral radiative heat flux below the upmost surface of half infinity solid domain 1 (i.e. $z = 0^+$ surface of the emitter), q''_1, can then be expressed with the following equation (3),

$$q''_1 = \frac{1}{2}\text{RE}\left[\int_0^\infty\int_0^\infty\int_0^\infty \left[\frac{1}{\omega\mu}|\boldsymbol{E}_{\text{TE}}(k_x,k_y,z')|^2 k_z^* + \frac{1}{\omega\varepsilon}|\boldsymbol{H}_{\text{TM}}(k_x,k_y,z')|^2 k_z\right] \text{d}k_x\text{d}k_y\text{d}z'\right]. \tag{3}$$

By using a generalized Wiener-Chaotic expansion technique, $|\boldsymbol{E}_{\text{TE}}(k_x,k_y,z')|$ and $|\boldsymbol{H}_{\text{TM}}(k_x,k_y,z')|$ can be determined as [12, 14]

$$|\boldsymbol{E}_{\text{TE}}(k_x,k_y,z')|^2 = \frac{1}{4\pi^3}\varepsilon_0\varepsilon''_1\Theta\frac{\omega^3\mu^2}{k_z k_z^*}\exp(-2k''_z z) \tag{4}$$

$$|\boldsymbol{H}_{\text{TM}}(k_x,k_y,z')|^2 = \frac{\omega}{4\pi^3}\varepsilon_0\varepsilon''_1\Theta\left(\frac{k_z k_z^* + k_x k_x + k_y k_y}{k_z k_z^*}\right) \times \exp(-2k''_z z) \tag{5}$$

with ε_0 the vacuum permittivity, ε the permittivity of the emitter equaling to $\varepsilon_0(\varepsilon_1' + i\varepsilon''_1)$, and $k_z = k'_z + ik''_z$ in the emitter. Θ is the mean energy of the Planck oscillator as $\Theta = \frac{\hbar\omega}{\exp(\hbar\omega/k_B T)-1}$ with $\hbar$ the reduced Planck constant and k_B the Boltzmann constant. Therefore, the spectral radiative heat flux $q''_1(\omega,T)$ near the surface of the hot emitter domain for a given emitter temperature T can be reorganized and expressed as follows by inserting equations (4) and (5) into equation (3) with $k''_z = \varepsilon''_1\varepsilon_0\mu\omega^2/2k'_z$ and $\left(k_z k_z^* + k_x k_x + k_y k_y\right)k'_z/\mu\omega^2 = \text{RE}[\varepsilon k_z^*]$,

$$q''_1(\omega,T) = \frac{1}{2}\Theta(\omega,T)\times\left[\int_0^\infty\int_0^\infty\left[\frac{1}{4\pi^3}\text{RE}\left[\frac{k'_z}{k_z}\right] + \frac{1}{4\pi^3}\text{RE}\left[\frac{\text{RE}[\varepsilon k_z^*]}{\varepsilon k_z^*}\right]\right]\text{d}k_x\text{d}k_y\right]. \tag{6}$$

When the radiative heat flux is transported from an emitter to a parallel collector across a gap with/without dielectric optical resonators, the transported radiative heat flux q''_{1-2} can be expressed as [13]

$$q''_{1-2}(\omega,T) = \frac{1}{8\pi^3}\Theta(\omega,T)\left[\int_0^\infty\int_0^\infty\left[\text{RE}\left[\frac{k'_z}{k_z}\right]F_{\text{TE}}(k_x,k_y) + \text{RE}\left[\frac{\text{RE}[\varepsilon k_z^*]}{\varepsilon k_z^*}\right]F_{\text{TM}}(k_x,k_y)\right]\text{d}k_x\text{d}k_y\right] \tag{7}$$

subscript 1 and 2 referring to domain 1 and domain 2;$F_{\text{TE}}(k_x,k_y)$ and $F_{\text{TM}}(k_x,k_y)$ the radiation power ratio at $z = d^-$ (just arriving at the collector) and $z = 0^+$ (before leaving the emitter) surfaces of figure 1 in TE or TM modes, respectively. $\text{RE}\left[\frac{k'_{1z}}{k_z}\right]F_{\text{TE}}(k_x,k_y)$ and $\frac{1}{8\pi^3}\Theta(\omega,T)$, are defined

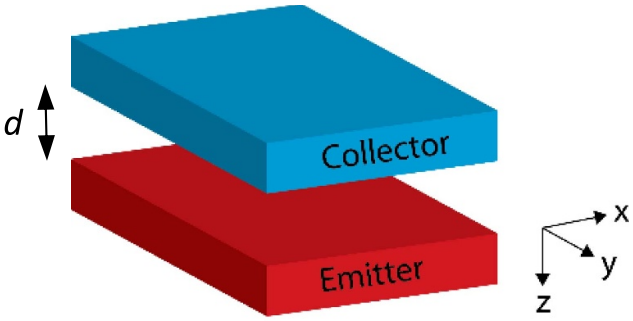

Figure 1. Illustration of the coordinate system. 'd' is the separation distance between the hot emitter and the cold collector [12]. Reproduced with permission from [13].

as normalized directional spectral radiation intensity in TE and TM mode (i.e. NDR_{TE} and NDR_{TM}), respectively, considering $\frac{1}{8\pi^3}\Theta(\omega,T)$ is the directional spectral radiation intensity from a blackbody. In other words, $\frac{1}{8\pi^3}\Theta(\omega,T)$ is used to normalize the direction spectral radiation intensity of near-field radiation for the following data analysis. $F_{TE}(k_x,k_y)$ and $F_{TM}(k_x,k_y)$ values are determined with scattering matrix methods [13, 15–18]. Because of the axial (or circular) symmetry of geometries in this study, we can use the results of $k_y = 0$ to demonstrate the full characteristic of the system [12, 14, 19, 20].

3. Results and discussions

With the scattering matrix approach, we first determine the NDR_{TE} and NDR_{TM} from a dielectric emitter to a dielectric collector in a configuration similar to figure 1. Both mediums are semi-infinitely large with a constant refractive index n equal to $6 + 0.001$i. $n = 6$ is among the largest value of infrared dielectric material [21]. The very small imaginary part of the dielectric constant is added to the emitter/collector domain to have intrinsic thermal radiation when the temperature is larger than 0 K [22]. Figure 2 shows the NDR_{TE} and NDR_{TM} when the separation distance of the two semi-infinite dielectric domains is equal to 10 nm or 100 nm. As in figure 2, the radiation intensity is mainly within the light cone of $n = 6$. NDR_{TE} is stronger than NDR_{TM} for large parallel wavenumber k_x. When the separation distance between the two semi-infinite domains is increased to 100 nm, NDR_{TE} becomes weak except for low frequencies for which the thermal radiation wavelength is still much larger than the 100 nm separation distance. The very small NDR_{TE} for higher frequencies in figure 2(c) can be understood with the very high reflectivity and the associated very low absorptivity/emissivity of a very high refractive index domain adopted in this study. NDR_{TM} shows a similar trend with very small radiation intensity between two high refractive index domains having a 100 nm separation (figure 2(d)). One unique characteristic of the NDR_{TM} is the extraordinarily large value close the Brewster's angle when the reflectivity is nearly zero. The characteristics observed in figure 2 from the scattering matrix analysis agree with solutions from the analytical solution of near-field thermal radiation. [22]

Next, we add a single dielectric thin film providing anti-reflection type resonance through anti-symmetric Fabry–Perot resonance as in figure 3 [11]. The refractive index n of dielectric films to achieve anti-reflection follows the thin film theory. [23] The thickness of the dielectric thin film determining cut-off resonance frequency is $\lambda/4n$ based on the design of anti-reflection coating. $\lambda = 2$ μm is adopted in this study, among the longest near-infrared wavelength in thermophotovoltaic applications. Figure 4 presents the NDR_{TE} and NDR_{TM} between two semi-infinite domains with the additional thin anti-reflection coating.

The thin anti-reflection dielectric film supports strong NDR_{TE} and NDR_{TM} outside of the light cone of a vacuum (i.e. the solid red line in figure 4). However, the dispersion relations of strong radiation are different for TE and TM polarizations. Large NDR_{TE} is confined to two well-separated bands in figure 4(a). In addition to the two main dispersion bands, enhanced near-field radiation can be observed at a very low frequency when the wavelength of the thermal radiation is much larger than the 100 nm gap. On the other hand, the dispersion relations for the large NDR_{TM} do not show such strong confinement into two separated bands as in the NDR_{TE}, and more dispersion curves are presented in figure 4(b). Also, the NDR_{TM} is significantly weaker than NDR_{TE} for larger parallel wavenumber k_x values. Field distribution from the emitter to the collector across the anti-reflection films is determined with the finite element method (FEM), as in figure 3.

As illustrated in figure 3, the resonance field in the anti-reflection coating is much stronger than the tunneled field in the collector from the emitter across the vacuum gap in TE mode. On the other hand, the resonance field in the anti-reflection coating has a similar magnitude as the tunneled field in the collector domain for TM mode radiation. The larger reflectivity values at the two interfaces of the anti-reflection coating under the TE mode radiation compared with that under the TM mode could be the reason for the stronger resonance field and associated stronger thermal field amplification/photon tunneling at a larger k_x value under the TE mode radiation. Note that for both TE and TM modes, the near field thermal photon tunneling is mainly confined within the light cone for $n = 2.45$ because the field resonance inside dielectric structures requires propagation of electromagnetic waves. Rhe refractive index of the thin dielectric film should be increased to extend k_x values allowing strong thermal photon tunneling. However, thin film anti-reflection coatings cannot have a very high refractive index based on the required impedance matching condition.

Thus, we examined the second approach to enhance thermal photon tunneling distance with pure dielectric structures by adding a lossless thin film with $n = 6$ on top of the dielectric domains, as illustrated in figure 5. The $n = 6$ high refractive index film (e.g. with GeSbTe [21]) can allow thermal electric propagation, amplification, and thermal photon tunneling at large k_x values. Note that the thin film cannot directly contact the dielectric emitter/collector. Otherwise, the NDR_{TE}

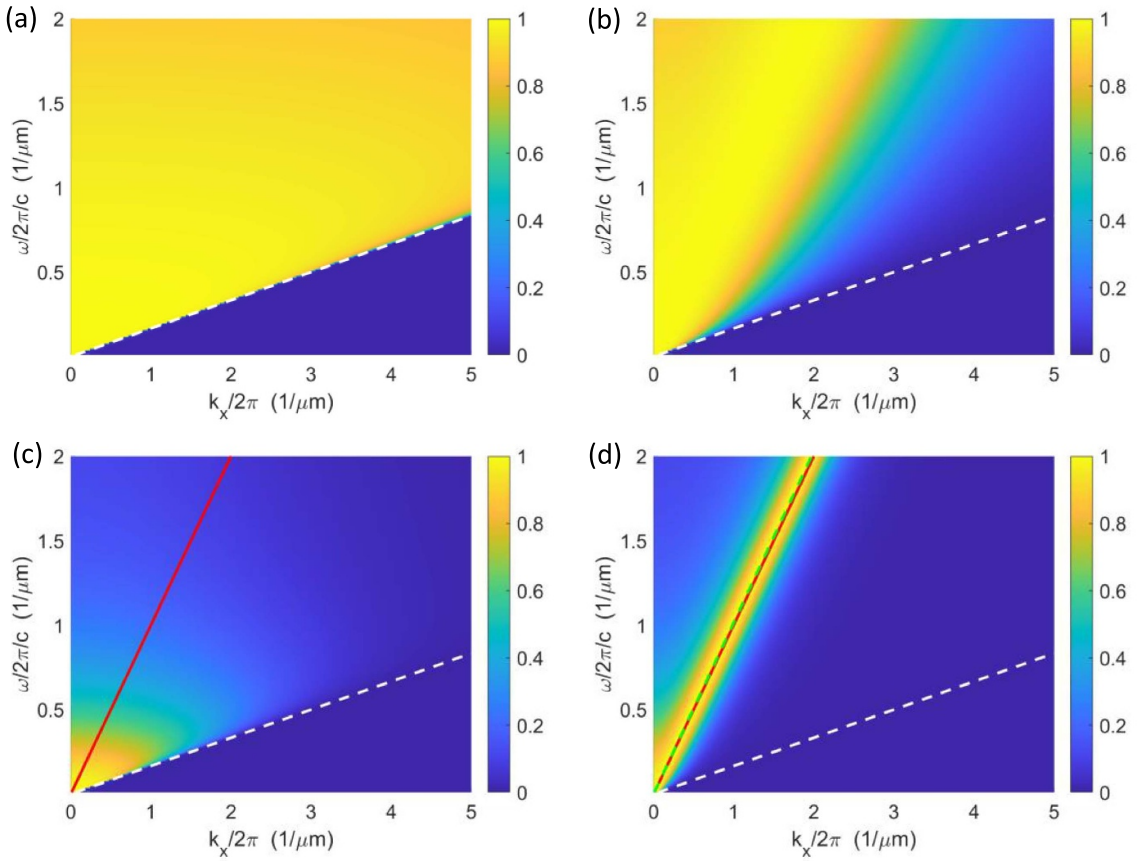

Figure 2. Near field radiation between two semi-infinite large domains with refractive index $n = 6 + 0001$i. (a) $\mathrm{NDR_{TE}}$ when two domains have a 10 nm separation, (b) $\mathrm{NDR_{TM}}$ when two domains have a 10 nm separation, (c) $\mathrm{NDR_{TE}}$ when two domains have a 100 nm separation, and (d) $\mathrm{NDR_{TM}}$ when two domains have a 100 nm separation. White dashed line indicates the light line of an $n = 6$ medium. Solid red line indicates the light line in a vacuum. Green dashed line indicates Brewster's angle.

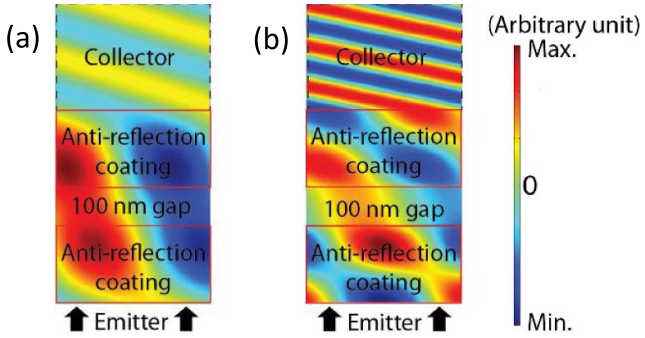

Figure 3. Geometry and field distribution from the emitter to the collector with anti-reflection coatings. (a) E_z value during TE thermal electric field transport when $\omega/2\pi c = 1(1\,\mu\mathrm{m}^{-1})$ and $k_x/2\pi = 1.82(1\,\mu\mathrm{m}^{-1})$, (b) H_z value during TM thermal electric field transport when $\omega/2\pi c = 1.6(1\,\mu\mathrm{m}^{-1})$ and $k_x/2\pi = 2(1\,\mu\mathrm{m}^{-1})$.

and $\mathrm{NDR_{TM}}$ will be the same as those in figure 2. A 30 nm gap is selected in this study between the $n = 6$ thin film and the top surface of the emitter/collector after several tests to have good coupling efficiency. The 30 nm gap can be maintained with porous low refractive index structures having a refractive index very close to one [24]. As a simplification, the refractive index of the 30 nm gap is equal to one in all calculations. We expect the additional $n = 6$ thin film slightly away from the dielectric emitter/collector can support the propagation of the electric field in its waveguide mode. Converting the coupled thermal electric field from the emitter to propagating modes of the thin film can accumulate and amplify the thermal electric field at the thin film, similar to the surface plasmon of conductive material. Thus, strong thermal photon tunneling can happen across a 100 nm gap, as in the previous case using anti-reflection coatings. The film thickness is equal to $\lambda/4n$ with $n = 6$ and $\lambda = 2$ μm in figure 5.

Figure 6 shows the $\mathrm{NDR_{TE}}$ and $\mathrm{NDR_{TM}}$ between the emitter and the collector with the addition of $n = 6$ thin film. The dispersion curves showing strong radiative energy transfer from the emitter to the collector domain correspond to the waveguide modes in the $n = 6$ film at 30 nm away from the emitter/collector. Because the $n = 6$ film has a higher refractive index than the anti-reflection film in the previous case, strong near-field photon tunneling can happen at larger k_x values for given frequencies. Moreover, TM has an additional strong photon tunneling dispersion curve along Brewster's

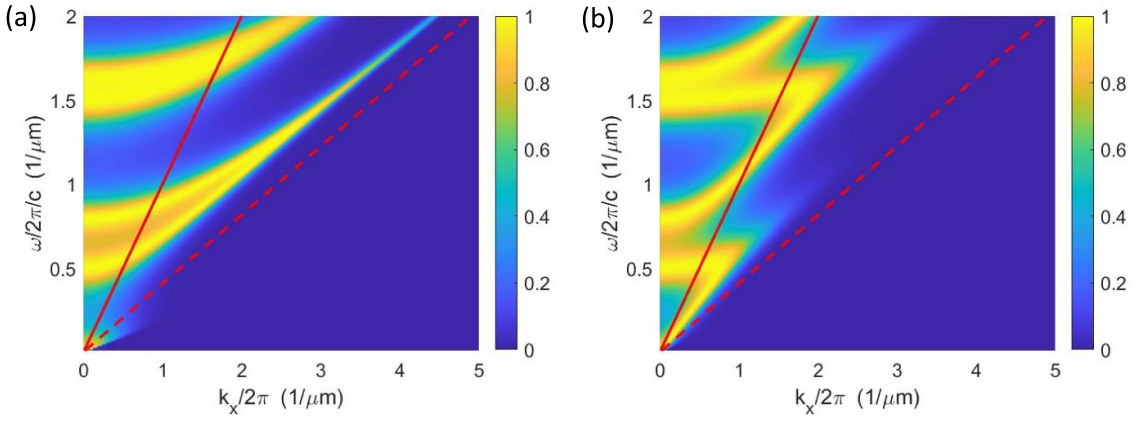

Figure 4. Near field radiation between two semi-infinite large domains with refractive index $n = 6 + 0001i$ having a thin anti-reflecting film coating. (a) NDR_{TE} when two domains have a 100 nm separation and (b) NDR_{TM} mode when two domains have a 100 nm separation. Red dashed line indicates the light line of an $n = 2.45$ medium.

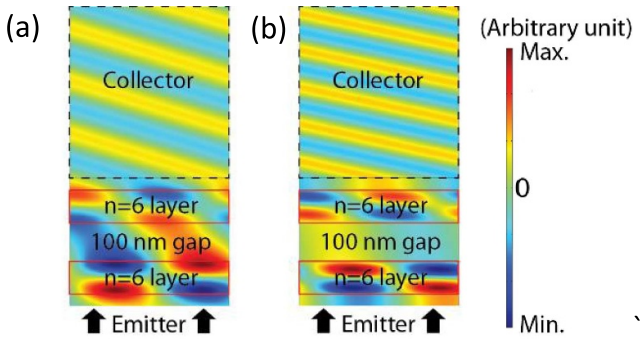

Figure 5. Geometry and field distribution from the emitter to the collector with one $n = 6$ layer. (a) E_z value during TE thermal electric field transport when $\omega/2\pi c = 1.3(1\,\mu m^{-1})$ and $k_x/2\pi = 2.3(1\,\mu m^{-1})$, (b) H_z value during TM thermal electric field transport when $\omega/2\pi c = 1.8(1\,\mu m^{-1})$ and $k_x/2\pi = 2.3(1\,\mu m^{-1})$.

angle, as in figure 2(b), due to the nearly zero reflection. Note that the trends of the dispersion curves of strong NDR_{TE} and NDR_{TM} show similar characteristics with transmission band edges of 1D photonic crystals for both the TE and TM mode radiations. The FEM is applied to better understand the field distribution from the emitter to the collector domain during enhanced photon tunneling due to the presence of a single layer $n = 6$ film. FEM results in figure 5 show the periodic variation of the electromagnetic field as propagation waves along the $n = 6$ film under the selected photon tunneling condition have much stronger strength than the tunneled field in the collector domain. Because the selected photon tunneling conditions are at the upper branch of the dispersion curves in figure 6, a full period of the electromagnetic field (i.e. varying from red to blue) can be observed along the vertical direction of the $n = 6$ films.

Considering the number of propagation modes is proportional to the thickness of a slab-type waveguide, we then triple the thickness of the $n = 6$ film to study the effects on the number of dispersion curves showing strong radiative energy transport. Figure 7 shows the NDR_{TE} and NDR_{TM} between the two dielectric domains with a single layer of $n = 6$ film having a thickness of 250 nm. The numbers of dispersion curves showing strong radiative energy transport are three times more than the numbers in figure 6. Also, each dispersion curve in figure 7 is narrower (i.e. more confined) than those in figure 6.

Because the dispersion relation of strong radiative energy transfer is similar to the transmission band edges of 1D photonic crystals, it is interesting to test whether the field amplification is also proportional to the number of $n = 6$ films as in Bloch surface waves of 1D photonic crystals [25]. Figure 9 shows the simulated NDR_{TE} and NDR_{TM} between the full dielectric emitter/collector domain separated by a 300 nm distance when 1, 2 and 3 layers of $n = 6$ coatings are added on top of the emitter/collector domain as in figure 8.

If we use $\omega/2\pi c \sim 1.1\,(1\,\mu m^{-1})$ for TE mode radiation and $\omega/2\pi c \sim 0.9\,(1\,\mu m^{-1})$ for TM mode radiation as examples, the photon tunneling strength at large k_x values increases with respect to the number of $n = 6$ layers on top of the emitter/collector domain. Each $n = 6$ layer has a 30 nm vacuum separation with the nearby layers, as in figure 8. Also observed is the increased number of dispersion curves showing strong radiative transport between the two dielectric domains when the number of $n = 6$ layer on the emitter/-collector domain is increased. Such an increase in propagation modes with respect to the number of high-low index layers is present in other 1D hyperbolic materials with laminate structures [26].

Figure 8 shows the field distribution from the emitter to the collector when three layers of $n = 6$ coatings are added on top of the emitter/collector surfaces, determined with the FEM method (figure 8). Based on the obtained field distribution, field strength in the $n = 6$ coatings increases when they are away from the emitter surface at conditions of strong near-field photon tunneling. This trend is more obvious if we compare the field intensity at the first and the third layer of the $n = 6$ films adjacent to the emitter. Such field amplification trend is similar to that at the surface of a truncated 1D photonic crystal supporting Bloch surface waves.

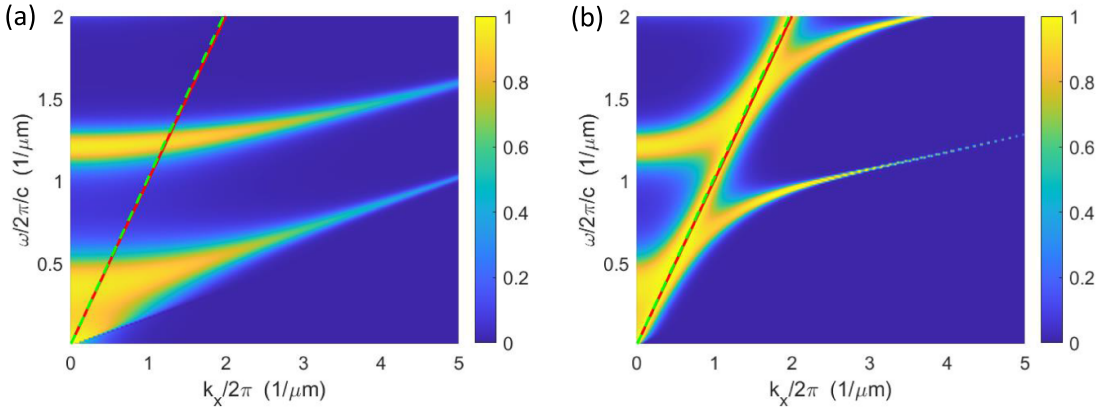

Figure 6. Near field radiation between two semi-infinite large domains with refractive index $n = 6 + 0001\mathrm{i}$ having a layer of $n = 6$ dielectric film with a thickness equal to 83.333 nm at a 30 nm distance away from the emitter/collector domain. (a) $\mathrm{NDR_{TE}}$ when two domains have a 100 nm separation and (b) $\mathrm{NDR_{TM}}$ when two domains have a 100 nm separation. The broken dispersion lines in (b) plot are because of the x and y resolution (200×500) of the simulation.

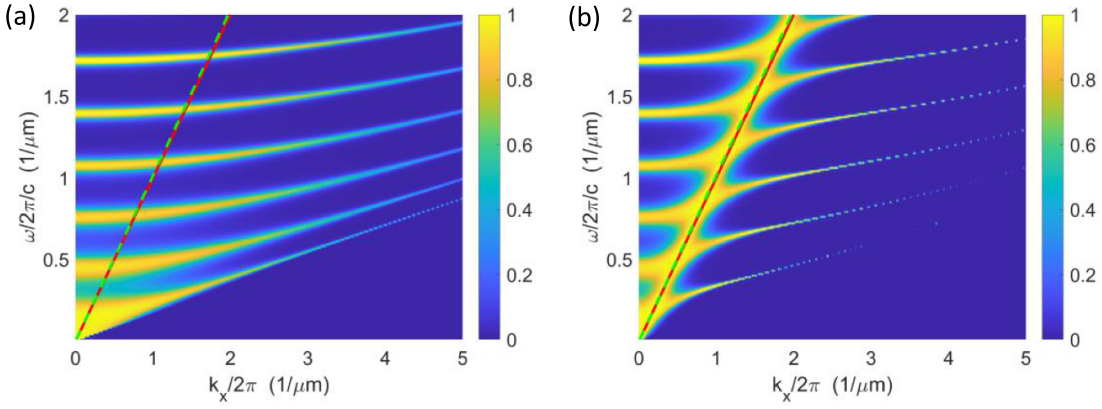

Figure 7. Near field radiation between two semi-infinite large domains with refractive index $n = 6 + 0001\mathrm{i}$ having $n = 6$ dielectric films with a thickness of 250 nm at a 30 nm distance away from the emitter/collector domain. (a) $\mathrm{NDR_{TE}}$ when two domains have a 100 nm separation and (b) $\mathrm{NDR_{TM}}$ when two domains have a 100 nm separation.

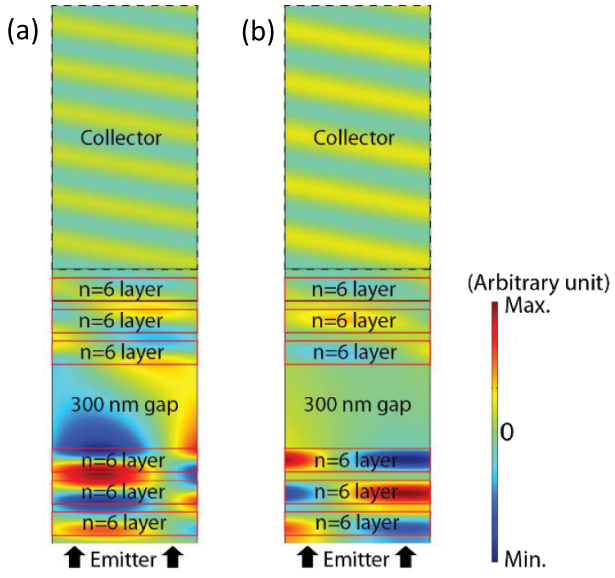

Figure 8. Geometry and field distribution when the emitter/collector with three $n = 6$ layers under photon tunneling conditions. (a) E_z value during TE thermal electric field transport when $\omega/2\pi c = 1.1(1\,\mu m^{-1})$ and $k_x/2\pi = 1.4(1\,\mu\mathrm{m}^{-1})$, (b) H_z value during TM thermal electric field transport when $\omega/2\pi c = 0.93(1\,\mu\mathrm{m}^{-1})$ and $k_x/2\pi = 1.25(1\mu\mathrm{m}^{-1})$.

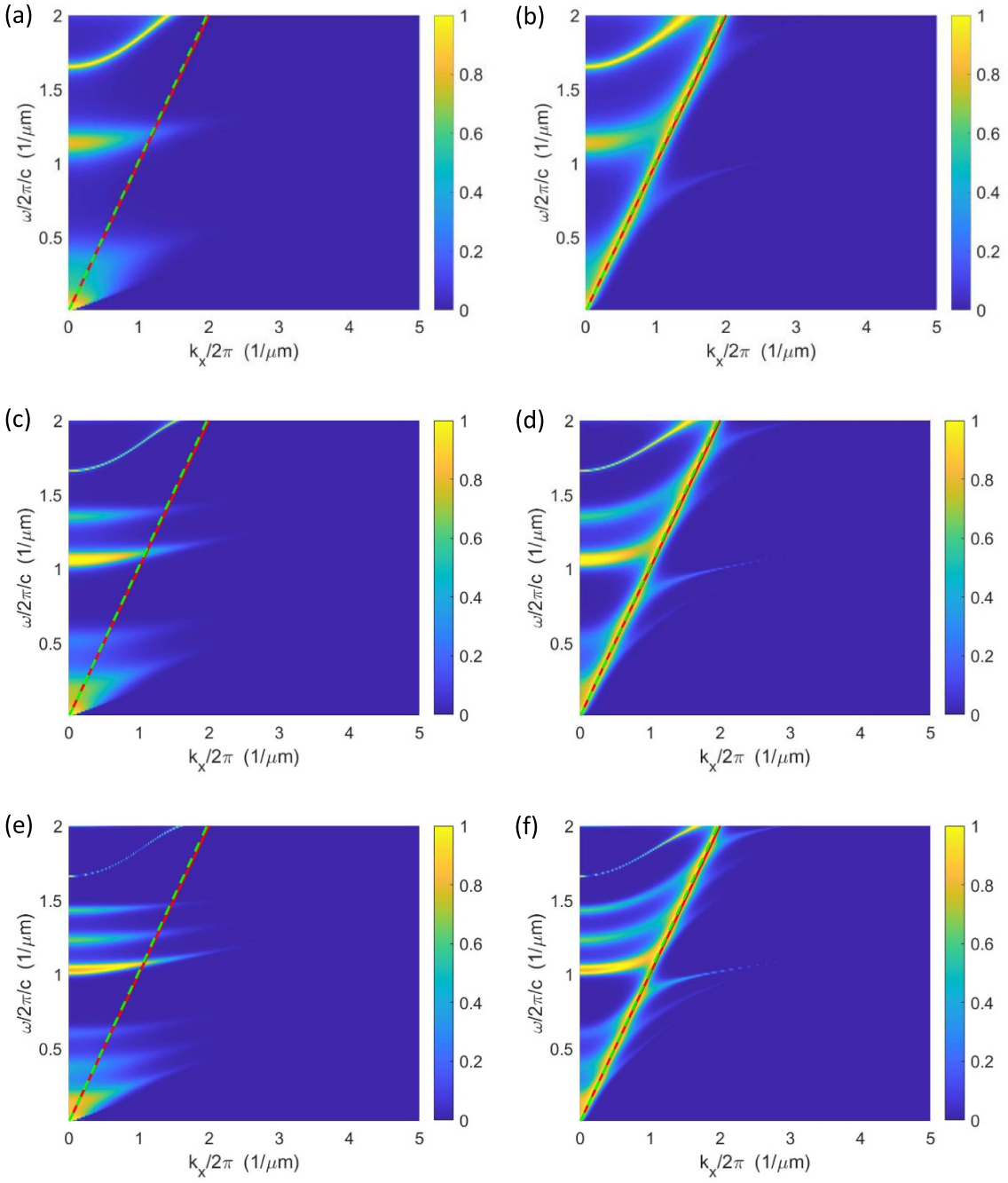

Figure 9. Near field radiation between two semi-infinite large domains with refractive index $n = 6 + 0001\mathrm{i}$ and multiple top layers of $n = 6$ dielectric films. Each layer of the $n = 6$ dielectric films is 83.333 nm thick and has a 30 nm separation distance from adjacent layers. Between the emitter and the collector is a 300 nm vacuum gap (compared with a 100 nm vacuum gap in previous cases). (a) $\mathrm{NDR_{TE}}$ results with one layer of $n = 6$ dielectric film on the emitter/collector, (b) $\mathrm{NDR_{TM}}$ results with one layer of $n = 6$ dielectric film on the emitter/collector, (c) $\mathrm{NDR_{TE}}$ results with two layers of $n = 6$ dielectric film on the emitter/collector, (d) $\mathrm{NDR_{TM}}$ results with two layers of $n = 6$ dielectric film on the emitter/collector, (e) $\mathrm{NDR_{TE}}$ results with three layers of $n = 6$ dielectric film on the emitter/collector, and (f) $\mathrm{NDR_{TM}}$ results with three layers of $n = 6$ dielectric film on the emitter/collector.

With the NDR vs. k_x relations presented in previous sections, we then determine the spectral emission power between the emitter and the collector with/without surface treatments such as anti-reflective coating (figure 5) or three-layered 1D photonic crystal type (figure 8) structures. Circular symmetry of the geometry and the resulting thermal radiation is applied to calculate the spectral emission power from $\mathrm{NDR}(\omega, k_x)$ when the vacuum gap between the emitter and collector domain is 100 nm. The obtained spectral emission power in figure 10 is normalized with the spectral emission power of a blackbody in TM or TE mode (i.e. $\frac{\hbar\omega^3}{8\pi^3c^2[\exp(\hbar\omega/k_BT)-1]}$). With no surface treatments, spectral emission power between the emitter and the collector is lower than blackbody radiation at high angular frequencies

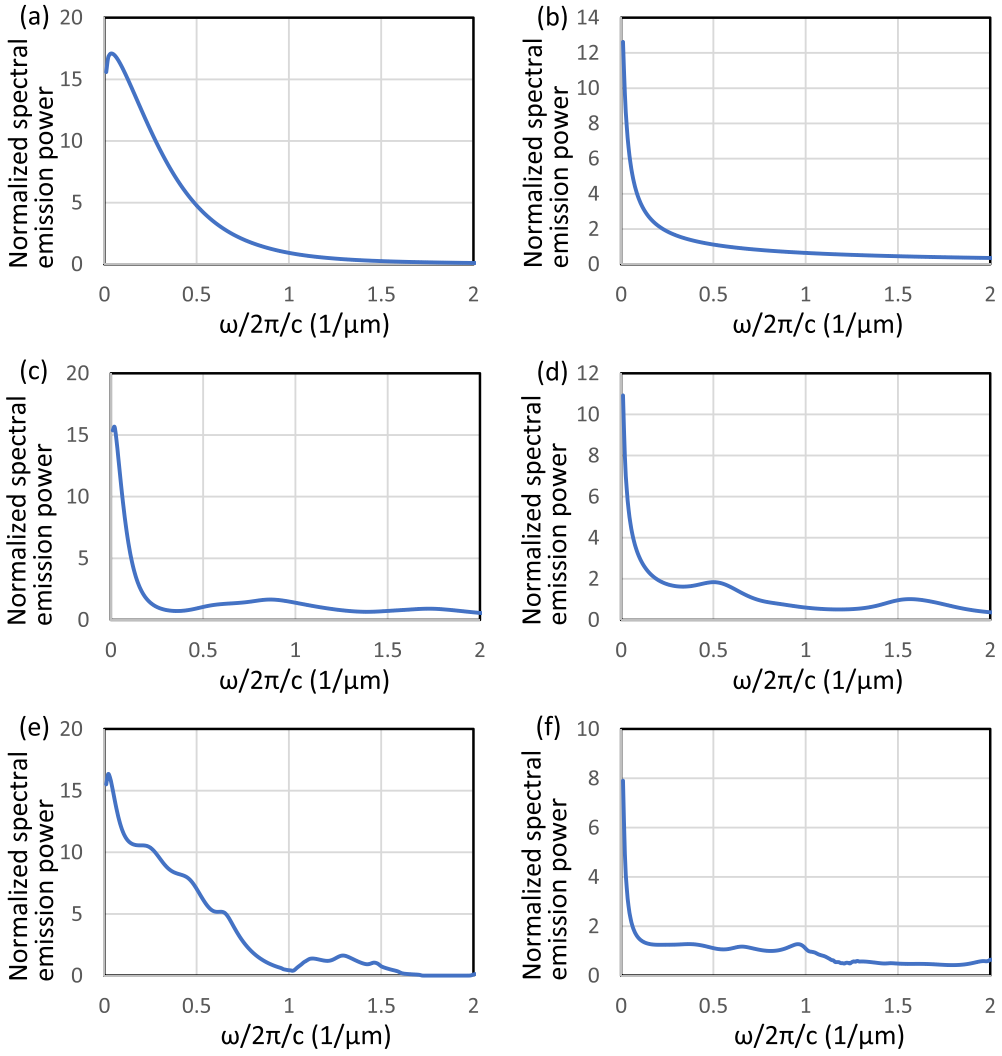

Figure 10. Spectral emission power between two semi-infinite large domains with refractive index $n = 6 + 0001i$ separated with a 100 nm vacuum gap. (a) TE mode radiation with no surface treatments on the emitter and the collector, (b) TM mode radiation with no surface treatments on the emitter and the collector, (c) TE mode radiation with anti-reflecting coating, as figure 5, on the emitter and the collector, (d) TM mode radiation with anti-reflecting coating, as figure 5, on the emitter and the collector, (e) TE mode radiation with three-layered 1D photonic crystal type structure, as figure 8, on the emitter and the collector, and (f) TM mode radiation with three-layered 1D photonic crystal type structure, as figure 8, on the emitter and the collector.

($\omega/2\pi/c > \sim 0.7$ for TE mode radiation and $\omega/2\pi/c > \sim 0.5$ for TM mode radiation) under which the radiation wavelength is short (figures 10(a) and (b)). When anti-reflective coatings are added, the spectral emission power is increased at the high angular frequencies (figures 10(c) and (d)), especially at the frequencies when optical resonance bands appear in figure 6. When three-layered 1D photonic crystal type structures are added, enhancements of spectral emission power are also present at the angular frequencies when resonance happens in the structure (figures 10(e) and (f)). The optical resonance bands of three-layered 1D photonic crystal type structures mainly happen at $\omega/2\pi/c < \sim 0.6$ or $\omega/2\pi/c > \sim 1$ for TE mode radiation. For TM mode radiation, the optical resonances shifts to $\omega/2\pi/c > \sim 0.5$, as in figure 9. Note that both the anti-reflective coating and three-layered 1D photonic crystal type structures can reduce the spectral radiation intensity between the emitter and the collector when no optical resonance happens in the additional thin film structures.

Calculations of spectral emission power are also performed by replacing the $n = 6$ collector with a GaSb PV cell commonly used in TPV cells to verify the ability of anti-reflecting coating and 1D photonic crystal type structures to enhance the performance of near field TPV devices. As illustrated in figure 11, the spectral emission power from the $n = 6$ emitter to the GaSb collector is also improved at similar angular frequencies when optical resonance happens, as in figure 10. The slightly reduced enhancement of the spectral radiation power in figure 11, compared with those in figure 10, is due to the non-symmetry of the emission and collection domain when the collector is replaced with the GaSb PV cell having a different refractive index with the emitter.

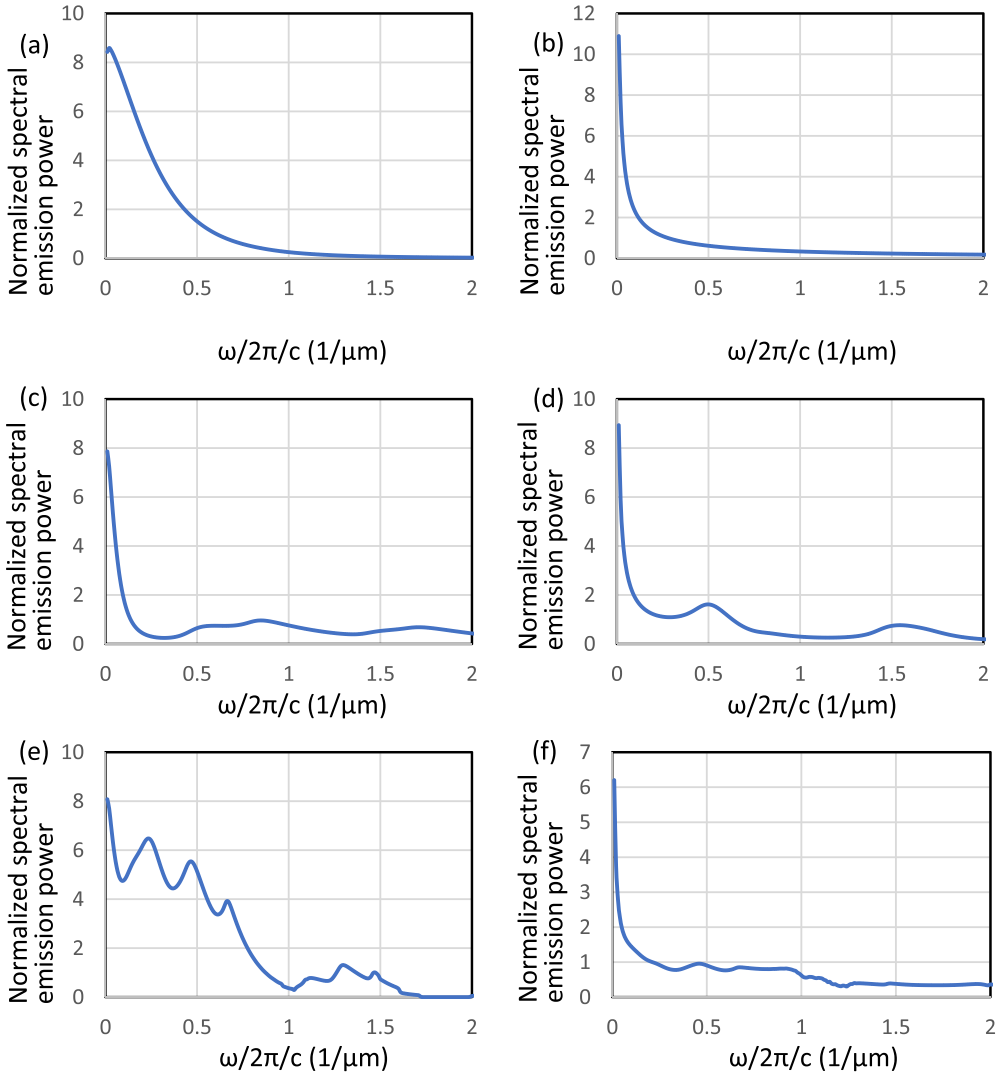

Figure 11. Spectral emission power between $n = 6 + 0001i$ emitter and a GaSb collector separated with a 100 nm vacuum gap. (a) TE mode radiation with no surface treatments on the emitter and the collector, (b) TM mode radiation with no surface treatments on the emitter and the collector, (c) TE mode radiation with anti-reflecting coating, as figure 5, on the emitter and the collector, (d) TM mode radiation with anti-reflecting coating, as figure 5, on the emitter and the collector, (e) TE mode radiation with three-layered 1D photonic crystal type structure, as figure 8, on the emitter and the collector, and (f) TM mode radiation with three-layered 1D photonic crystal type structure, as figure 8, on the emitter and the collector.

4. Conclusion

In conclusion, the high radiation intensity inside a high refractive dielectric material can tunnel across a >100 nm vacuum gap, which is valuable for different energy applications by using pure dielectric structures supporting field resonance and/or wave propagation. We successfully demonstrated that anti-symmetric Fabry–Perot resonance with anti-reflection coating and 1D photonic crystal type periodic high-low refractive index structures could be two of the choices that can amplify the thermal electric field on a dielectric domain for the longer distance thermal photon tunneling. The parallel wavenumber allowing field amplification and the thermal photon tunneling is determined by the refractive index of the pure dielectric structure supporting the field resonance and/or wave propagation. Compared with anti-symmetric Fabry–Perot resonance with anti-reflection coating, 1D photonic crystal type periodic structures can be constructed with higher refractive dielectric materials as the emitter/collector domain. Thus, 1D photonic crystal type periodic structures can be preferred in the long-distance tunneling of thermal photons from high refractive index emitters/collectors. Moreover, the amplification with the 1D photonic crystal type periodic structures is increased with respect to the number of high-low index layers. By using these characteristics, we expect chemically stable high intensity near field thermophotovoltaic devices having a 100's nm vacuum gap can be constructed with pure dielectric materials, which is feasible with current fabrication techniques. In real applications, we will design thin film structures having photon tunneling frequencies slightly higher than the band edge of the PV cells of the thermophotovoltaic devices. Thus, even with a small shift

of the actual photon tunneling frequencies, compared with the design due to the machining accuracy, the tunneled photons can still be absorbed by the PV cells as electricity output.

Data availability statement

The data that support the findings of this study are available from the corresponding author upon reasonable request.

Acknowledgment

The research is supported by National Science Foundation (CBET- 2117953).

ORCID iDs

Sy-Bor Wen https://orcid.org/0000-0001-8106-0918
Aravind Jakkinapalli https://orcid.org/0000-0001-6779-3867

References

[1] Sakakibara R, Stelmakh V, Chan W R, Ghebrebrhan M, Joannopoulos J D, Soljacic M and Celanovic I 2019 Practical emitters for thermophotovoltaics: a review *J. Photon. Energy* **9** 032713
[2] Würfel P and Würfel U 2009 *Physics of Solar Cells: From Basic Principles to Advanced Concepts* 2nd edn (Weinheim: Wiley-VCH)
[3] Howell J R, Mengüç M P, Daun K J and Siegel R 2021 *Thermal Radiation Heat Transfer* 7th edn (Boca Raton, FL: CRC Press)
[4] Hu L, Narayanaswamy A, Chen X Y and Chen G 2008 Near-field thermal radiation between two closely spaced glass plates exceeding Planck's blackbody radiation law *Appl. Phys. Lett.* **92** 133106
[5] Nemilentsau A M, Slepyan G Y and Maksimenko S A 2007 Near-field and far-field effects in thermal radiation from metallic carbon nanotubes *Proc. SPIE* **6728** 672809
[6] Luo C Y, Johnson S G, Soljacic M, Joannopouls J D and Pendry J B 2003 Novel optical phenomena with photonic crystals *Proc. SPIE* **5166** 207–19
[7] Basu S and Zhang Z M 2009 Maximum energy transfer in near-field thermal radiation at nanometer distances *J. Appl. Phys.* **105** 093535
[8] Wen S B and Jakkinapalli A 2021 Enhanced tunneling distance of near field radiative energy with high-index dielectric resonators *Appl. Phys. Lett.* **119** 234101
[9] Silva-Oelker G, Jerez-Hanckes C and Fay P 2018 Study of W/HfO_2 grating selective thermal emitters for thermophotovoltaic applications *Opt. Express* **26** A929–36
[10] Wang R X *et al* 2017 Diffraction-free Bloch surface waves *ACS Nano* **11** 5383–90
[11] Zhang X L, Song J F, Li X B, Feng J and Sun H B 2013 Anti-reflection resonance in distributed Bragg reflectors-based ultrathin highly absorbing dielectric and its application in solar cells *Appl. Phys. Lett.* **102** 103901
[12] Wen S B 2010 Direct numerical simulation of near field thermal radiation based on wiener chaos expansion of thermal fluctuating current *Trans. ASME, J. Heat Transfer* **132** 072704
[13] Wen S B and Jakkinapalli A 2022 5 μm level long photon tunneling distance in near field thermal radiation through metallic patterns with/without dielectric structures *Trans. ASME, J. Heat Transfer* **144** 112801
[14] Wen S B 2021 A simple approach to evaluate near field thermal radiation from emitters with layered structures and temperature variations in one direction *Trans. ASME, J. Heat Transfer* **143** 022801
[15] Li L F 1997 New formulation of the Fourier modal method for crossed surface-relief gratings *J. Opt. Soc. Am.* A **14** 2758–67
[16] Li L F 2003 Fourier modal method for crossed anisotropic gratings with arbitrary permittivity and permeability tensors *J. Opt. A: Pure Appl. Opt.* **5** 345–55
[17] Inoue T, Watanabe K, Asano T and Noda S 2018 Near-field thermophotovoltaic energy conversion using an intermediate transparent substrate *Opt. Express* **26** A192–208
[18] Liu X L, Zhao B and Zhang Z M M 2015 Enhanced near-field thermal radiation and reduced Casimir stiction between doped-Si gratings *Phys. Rev.* A **91** 062510
[19] Joulain K, Mulet J P, Marquier F, Carminati R and Greffet J J 2005 Surface electromagnetic waves thermally excited: radiative heat transfer, coherence properties and Casimir forces revisited in the near field *Surf. Sci. Rep.* **57** 59–112
[20] Mulet J P, Joulain K, Carminati R and Greffet J J 2002 Enhanced radiative heat transfer at nanometric distances *Microscale Thermophys. Eng.* **6** 209–22
[21] Krishnamoorthy H N S, Adamo G, Yin J, Savinov V, Zheludev N I and Soci C 2020 Infrared dielectric metamaterials from high refractive index chalcogenides *Nat. Commun.* **11** 1692
[22] Novotny L and Hecht B 2012 *Principles of Nano-Optics* 2nd edn (Cambridge: Cambridge University Press)
[23] Meyer-Arendt J R 1984 *Introduction to Classical and Modern Optics* 2nd edn (Englewood Cliffs, NJ: Prentice-Hall)
[24] Schubert E F and Kim J K 2009 Low-refractive-index materials—a new class of optical thin-film materials *2009 Conf. on Lasers and Electro-Optics and Quantum Electronics and Laser Science Conf. (Cleo/qels 2009)* vol 1–5 p 1359
[25] Gonzalez-Valencia E, Del Villar I and Torres P 2021 Novel Bloch wave excitation platform based on few-layer photonic crystal deposited on D-shaped optical fiber *Sci. Rep.* **11** 11266
[26] Biehs S A and Ben-Abdallah P 2017 Near-field heat transfer between multilayer hyperbolic metamaterials *Z. Naturforsch.* A **72** 115–27